

# Planar Photonic Crystal Nanolasers (I): Porous Cavity Lasers

Marko LONČAR<sup>†a)</sup>, Tomoyuki YOSHIE<sup>††</sup>, Koichi OKAMOTO<sup>††</sup>, Yueming QIU<sup>†††</sup>, Jelena VUČKOVIĆ<sup>††††</sup>,  
and Axel SCHERER<sup>††</sup>, *Nonmembers*

**SUMMARY** We have designed, fabricated and characterized efficient optical resonators and low-threshold lasers based on planar photonic crystal concept. Lasers with InGaAsP quantum well active material emitting at 1550 nm were optically pumped, and room temperature lasing was observed at threshold powers below 220  $\mu$ W. Porous high quality factor cavity that we have developed confines light in the air region and therefore our lasers are ideally suited for investigation of interaction between light and matter on a nanoscale level. We have demonstrated the operation of photonic crystal lasers in different ambient organic solutions, and we have showed that planar photonic crystal lasers can be used to perform spectroscopic tests on femtoliter volumes of analyte.

**key words:** photonic crystals, photonic bandgap, laser, nanophotonics, nanofabrication, FDTD

## 1. Introduction

Photonics has recently become an attractive alternative to electronics technology owing to advantages offered by information processing in the optical domain (high speed, wide bandwidth, reduced cross-talk). At the same time, nanotechnology, technology that was driven by the ever-growing need to shrink the sizes of electronic devices, has evolved to a precision which allows us to create nanoscale structures in a reproducible and controllable manner. By combining the need for integrated photonics with the promise of nanotechnology, a field of *Nanophotonics* has emerged. Nanophotonics devices, defined in conventional microelectronics materials, can be highly integrated thus achieving the dream of large-scale integrated all-optical systems. In addition, they can be integrated with electronic components resulting in hybrid systems of higher complexity. On the other hand, nanoscale photonic structures offer a great promise for the investigation of fundamental physical laws that govern the behavior of photons on a nanoscale level.

The photonic crystal [1],[2] (PC) is one of the

---

Manuscript received August 4, 2003.

Manuscript revised October 9, 2003.

<sup>†</sup>The author is with the Division of Engineering and Applied Sciences, Harvard University, 9 Oxford Street, Cambridge, MA 02138, USA.

<sup>††</sup>The authors are with the Department of Electrical Engineering, California Institute of Technology, MS 136-93, Pasadena, CA 91125, USA.

<sup>†††</sup>The author is with In Situ Technology and Experiments Systems Section, Jet Propulsion Laboratory, MS 302-306, Pasadena, CA 91109, USA.

<sup>††††</sup>The author is with Ginzton Laboratory, Stanford University, Stanford, CA 94305-4088, USA.

a) E-mail: loncar@deas.harvard.edu

nanophotonics platforms that can enable the miniaturization of photonic devices and their large-scale integration. These man-made periodic nano-structures can be designed to form frequency bands (photonic bandgaps) within which the propagation of electromagnetic waves is forbidden irrespective of the propagation direction. By making the spatial periodicity in three dimensions (3-D), it is possible to control the flow of light completely. However, fabrication of 3-D PC structures is still a difficult process, and a more appealing approach is based on the use of lower-dimensional photonic crystals. A structure that has recently attracted a lot of attention is a semiconductor membrane perforated with 2-D lattice of holes [3]. The big advantage of these planar photonic crystals (PPC) is that their fabrication procedure is compatible with planar technology used to realize micro-electronic systems, and it allows for lithographic tunability of the devices.

One of the most promising applications of planar photonic crystals is the realization of a compact and efficient optical nanocavity, with high quality factor ( $Q$ ) and small mode volume ( $V_{mode}$ ). Such a nanoscale optical resonator is of interest for a number of applications including realization of low-threshold lasers [4]–[12], biochemical sensors [13], add/drop filters for WDM applications [14], strong coupling cavity QED experiments [15],[16], etc. In this work we are interested in high- $Q$  optical nano-resonators that concentrate light in the air and therefore are natural candidates for investigation of interaction between light and matter placed into the high optical fields.

## 2. High-Q Cavity Design

Photonic crystal cavities can be formed by modifying one or more holes in the photonic crystal lattice. By making one of the holes smaller (donor-type cavity) we locally decrease the amount of low-dielectric constant material (air) and thereby reduce the energy of the modes supported in the bulk photonic crystal. Modes that were originally confined in the air (air band modes) will now be pulled down into the band gap, and be trapped in the energy well formed by reducing the size of the hole. Similarly, by increasing the size of one of the holes (acceptor-type cavity), we form bound states close to the dielectric (valence) band (Fig. 1).

The efficiency of a resonator, described by a quality factor ( $Q$ ), can be expressed as the ratio of energy stored in the cavity and energy lost (emitted) from the cavity in one

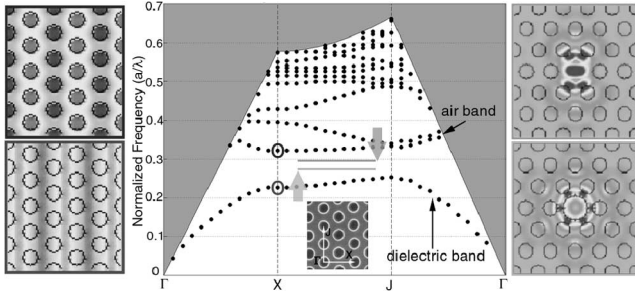


**Fig. 1** Band diagram for the modes supported in the triangular lattice planar photonic crystal ( $r/a = 0.3$ ). Distribution of the  $E$ -field in the case of air and dielectric band is shown to the left, and mode profile of donor and acceptor cavity to the right.

cycle

$$Q = 2\pi \frac{W_{\text{stored}}}{W_{\text{lost}}} \quad (1)$$

In case of 3-D photonic crystal, with infinitely many PC layers around the defect, light can be completely trapped to the defect. However, in cavities defined in photonic crystal slabs, modes will suffer from radiation losses due to the coupling into the continuum of radiation modes that exist within the light cone. These components contribute to the *out-of-plane* losses of the cavity. At the same time, light can leak laterally due to the finite number of the photonic crystal layers surrounding the cavity, contributing to the *in-plane* losses of the resonator. Therefore, the quality factor of the cavity can be broken into lateral quality factor ( $Q_{\text{lat}}$ ) and vertical quality factor ( $Q_{\text{vert}}$ ) that take into account in-plane and out-of-plane losses, respectively.

$$\frac{1}{Q} = \frac{1}{Q_{\text{lat}}} + \frac{1}{Q_{\text{vert}}} \quad (2)$$

By adding more photonic crystal layers around the cavity, the lateral leak can be completely suppressed, and the ultimate  $Q$  is limited by  $Q_{\text{vert}}$  [17]. The simplest photonic crystal cavity, formed by reducing the size of one of the holes (single defect cavity), suffers from large radiative losses and modest  $Q_{\text{vert}} \approx 2000$  can be achieved when  $r/a = 0.275$  and  $r_{\text{def}}/a = 0.2$  [15]. In addition, this cavity design is not robust since the defect hole is only slightly smaller than bulk photonic crystal holes, and any fabrication disorders can spoil  $Q$  factor. The problem of high- $Q$  cavity design has recently attracted a lot of research attention and several designs were proposed [7], [9], [15], [18]–[20].

The high- $Q$  cavity geometry that we proposed is based on fractional edge dislocations in the single defect triangular lattice photonic crystal [15]. Our planar photonic crystal is based on a free-standing membrane: high dielectric constant slab (refractive index  $n = 3.4$ ) is perforated with 2-D lattice of holes with periodicity  $a$  and is suspended in the air. The cavity consists of a defect hole (radius  $r_{\text{def}}$ ) that is smaller than surrounding holes (radius  $r$ ) which define the photonic crystal mirror. The row that contains the defect hole is elongated by moving two photonic crystal half-planes a fraction

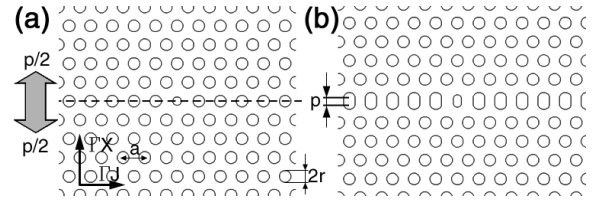


**Fig. 2** (a) Conventional single defect cavity ( $p = 0$ ). When structure is “cut” along the dashed line, and two PPC half-planes are dislocated along  $\Gamma X$  direction by  $p/2$ , (b) high- $Q$  cavity can be formed.

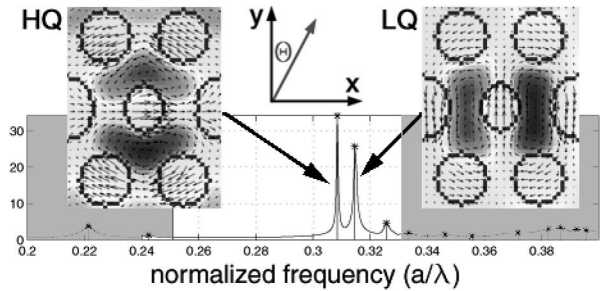


**Fig. 3** Cavity with  $p/a = 10\%$  and  $r_{\text{def}} = 0.2a$  supports two dipole modes, and their profiles are shown ( $B_z$  component and vector of the  $\vec{E}$  field). Spectrum of the modes supported in the cavity, obtained using 3-D FDTD, is also shown. The bandgap is shown in white.

of a lattice constant apart in the  $\Gamma X$  direction (Fig. 2). Each half-plane is moved by  $p/2$ , yielding total dislocation of  $p$ .

Three dimensional finite difference time domain (3-D FDTD) method [21] was used to analyze the cavities, and discretization used in FDTD algorithm was  $a = 20$  computational points. A single defect donor cavity in a triangular lattice photonic crystal without the fractional edge dislocation is known to support two doubly-degenerate, linearly polarized, dipole modes [17]. However, as we stretch the photonic crystal lattice by introducing a fractional dislocation, these modes start to interact and the degeneracy between them is lifted. In Fig. 3 we show the results of 3-D FDTD analysis of the structure with  $p/a = 10\%$ ,  $r_{\text{def}} = 0.2a$ ,  $r = 0.3a$  and thickness  $d = 0.75a$ . Two dipole modes, labelled LQ and HQ, are found to exist in the cavity. The mode at longer wavelength can have an order of magnitude better  $Q$  factor value and therefore is called HQ (high- $Q$ ) mode.

In Fig. 4 we show dependence of the  $Q$  factor of the HQ mode of the cavity on the dislocation, for  $r/a = 0.275$  and  $r_{\text{def}}/a = 0.2$ .  $Q$  factor better than 10000 can be achieved when elongation is  $p/a = 10\%^\dagger$ . This high  $Q$  value is obtained while maintaining a very small mode volume of  $V_{\text{mode}} \approx 0.1(\lambda/2)^3$ . Strong dependence of the cavity  $Q$  on the dislocation can be attributed to the tuning effect of the cavity length in order to accommodate the dipole mode of interest. Influence of dislocation can be completely understood by

<sup>†</sup>In Ref. [15] we showed that  $Q \approx 34000$  can be achieved when fractional edge dislocation is introduced in the holes along  $y$ -axis, and the size of four holes closest to the central defect hole is reduced to  $r'/a = 0.225$ .

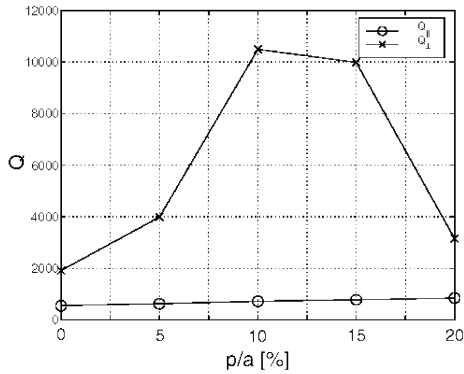


**Fig. 4**  $Q_{vert}$  as a function of dislocation  $p/a$ .  $r/a = 0.275$ ,  $r_{def}/a = 0.2$ ,  $n = 3.4$  and relative thickness of the slab  $d/a = 0.75$ .

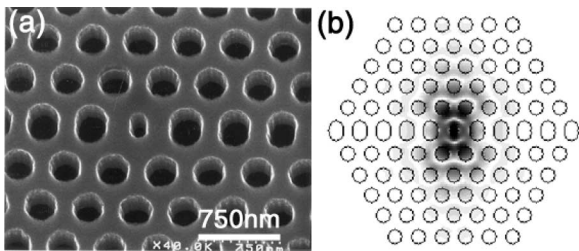


**Fig. 5** Scanning electron micrograph and calculated field distribution of our high-Q cavity.

conduction the analysis in reciprocal (Fourier) space [22].

Cavities based on fractional edge dislocation concentrate light in the air (Fig. 5) and therefore they are natural candidates for investigation of interaction between light and matter placed into high optical fields. These cavities were originally designed for cavity QED experiments, where strong-coupling between Cs atoms introduced into the high field region of the cavity and light trapped in the cavity was to be investigated [15]. Therefore, it was important to maintain rather large defect hole in order to facilitate the trapping of Cs atoms. Another application of this porous cavity design that we have proposed and demonstrated was realization of low-threshold laser [11] suitable for detection of biochemical reagents [13]. However, it is clear that the presence of a large hole at the point of maximum field intensity is not desirable in low-threshold laser designs, since the overlap with the gain region provided by quantum wells is decreased. Therefore, we have revisited the problem of cavity design in order to investigate the influence of the defect hole size ( $r_{def}$ ) on the Q factor of the cavity.

In order to improve the lateral confinement of light, we decided to analyze structures with slightly bigger holes ( $r/a = 0.3$ ). In Fig. 6 we show the dependence of the eigenfrequency and Q of HQ dipole mode on the stretching (dislocation) of the central row ( $p/a$ ) and on the size of the defect hole ( $r_{def}/a$ ). In our calculations, cavity was surrounded with five layers of photonic crystal, as shown in Fig. 5(b). It can be seen that by increasing the dislocation, the splitting between the two dipole modes increases. Also, as the

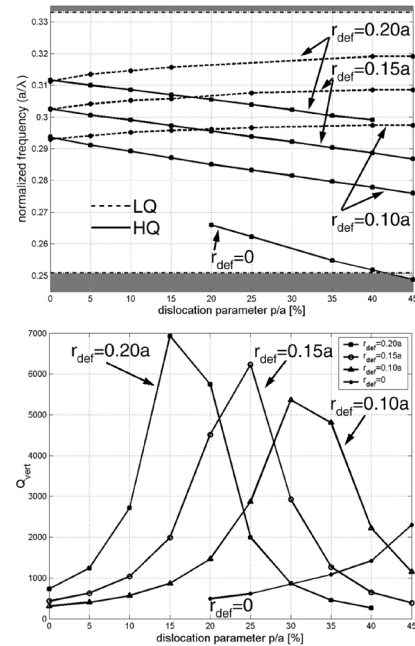


**Fig. 6** Dependence of the (a) frequency of HQ and LQ dipole modes and (b) Q-factor of HQ mode on the amount of dislocation and the size of the defect hole ( $r_{def}$ ).  $r/a = 0.3$ ,  $d/a = 0.75$ , and  $n_{slab} = 3.4$ . Bandgap exists in the range  $a/\lambda \in (0.2508, 0.3329)$ .

defect hole becomes larger the modes shift towards higher frequencies, due to an increased overlap between the optical field and air. The mode of interest for laser applications is the HQ mode, since it has an order of magnitude higher Q and therefore will reach threshold first. The best Q that we could achieve in the modelled cavity geometry is around 7000. In comparison, we were able to achieve Qs as high as 11000 when  $r/a = 0.275$ . As expected, due to the increased size of the bulk photonic crystal holes ( $r/a = 0.3$ ), light scattering in the vertical direction increases, and therefore the Q-factors are smaller. In order to increase the Q of the cavity, Fourier components of the mode that lie within the light cone need to be minimized [22]. This can be achieved by changing the size of the air-region in the cavity. The change of the area occupied by the defect hole, induced by stretching of the central row, is  $\Delta A = 2r_{def} \cdot p$ , and in order to achieve the same influence on the mode larger  $p$ 's are needed when  $r_{def}$  is made smaller. Therefore, the optimal design (Q-factor maximized) requires more dislocation as  $r_{def}$  decreases, as it can be seen in Fig. 6(b). For initial laser sensor design we have chosen  $r_{def} = 0.15a$  and  $p = 0.25a$  as a good compromise between gain provided in the cavity and relatively large defect hole air region where matter can be placed.

### 3. Low-Threshold Planar Photonic Crystal Nanolaser

In this section we explain the fabrication and experimental characterization of lasers based on our high-Q cavity, designed and fabricated in InGaAsP material system. InGaAsP quantum well material was grown on InP substrate

using metal-organic chemical vapor deposition (MOCVD). Optical gain is provided by four 9 nm thick, compressively strained, quantum wells with an electronic bandgap at  $\lambda_{bg} = 1.55 \mu\text{m}$ , separated by 20 nm thick InGaAsP barriers ( $\lambda_{bg} = 1.22 \mu\text{m}$ ). Because of the compressive strain, the coupling is the strongest to the TE polarized modes of the slab. This is desirable since in triangular lattice PPC the bandgap is larger for TE-polarized light. This active material is placed in the center of a 330 nm thick InGaAsP slab ( $\lambda_{bg} = 1.22 \mu\text{m}$ ), with 1  $\mu\text{m}$  thick sacrificial InP layer underneath the slab. An InGaAs etch stop is introduced above the InP substrate, and the active quaternary material is designed to operate at  $\lambda = 1.55 \mu\text{m}$ .

### 3.1 Fabrication Procedure

Fabrication procedure consists of electron-beam lithography, followed by several dry- and wet-etching steps. Ideally, only one mask layer would be needed to define patterns in InGaAsP material of interest. However, due to poor etching selectivity between e-beam resist and InGaAsP we had to use the *mask amplification* method. Initially, total of three mask layers were used before the patterns are defined in InGaAsP. An etch mask consists of 40 nm Au evaporated on top of 100 nm SiON, deposited using plasma enhanced CVD (PECVD). The fabrication process starts with the deposition of 150 nm of polymethyl methacrylate (PMMA) electron beam resist, followed by electron-beam lithography to define structures in PMMA. By varying the electron dose and the periodicity of the photonic crystal lattice during the e-beam lithography step, we could span the entire design space of the PPC nanocavities by changing  $a$ ,  $r$ ,  $r_{def}$  and  $p/a$  independently. We use  $\text{Ar}^+$  ion milling to transfer the mask pattern through the Au mask and follow this step by a  $\text{C}_2\text{F}_6$  reactive ion etching (RIE) to transfer the mask from the Au into the SiON. At the end, the patterns were transferred into the InGaAsP using inductive-coupled plasma RIE etching, using the mixture of Ar and Cl gases. Finally, the remaining SiON mask is removed in a HF acid and the InGaAsP membrane is released from the substrate by wet etching in 4:1 HCl:water solution at 4°C. HCl goes into the photonic crystal holes, and selectively attacks InP sacrificial layer, leaving InGaAsP membrane suspended in the air. In Fig. 7 we show some of the fabricated structures. Each pattern consists of six different cavities that have received the same electron-dose during the e-beam lithography step, and therefore should have similar hole size ( $r$ ) and lattice constant ( $a$ ). The only difference between the cavities in one structure is the value of the dislocation parameter  $p$  that assumed values in the range  $p/a \in (0, 0.25)$ .

In the second generation of lasers we have simplified the fabrication procedure by replacing  $\text{C}_2\text{F}_6$  gas with  $\text{CHF}_3$  during RIE step. Then, we were able to etch SiON using PMMA as the only mask, and Au mask layer and milling step were not necessary any more. The final structure, made using modified fabrication procedure, is shown in Fig. 8(a) and distribution of hole radii is shown in Fig. 8(b). The

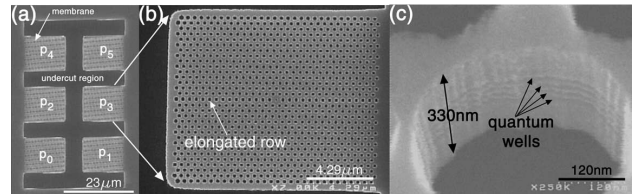


**Fig. 7** SEM micrograph of one of the fabricated structures. Each structure consists of (a) six different cavities with different elongation parameters:  $p_0 = 0$ ,  $p_1 = 0.05 \cdot a$ ,  $p_2 = 0.1 \cdot a$ ,  $p_3 = 0.15 \cdot a$ ,  $p_4 = 0.2 \cdot a$  and  $p_5 = 0.25 \cdot a$ . (b) Blow-up of  $p_3$  cavity, and (c) of a single hole (tilted). Quantum wells and undercut air region can be seen.

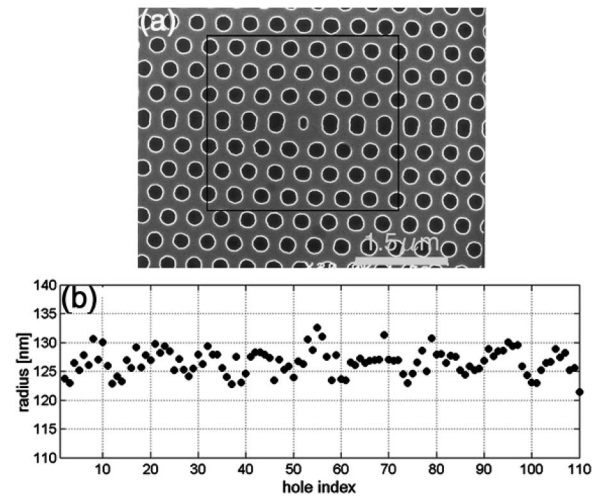


**Fig. 8** (a) SEM micrograph of one of the fabricated structure and (b) distribution of the radii of the holes in photonic crystal mirror (defect hole and elongated holes are not shown). Hole 1 is in top left corner, and hole 110 in bottom right corner (hole 12 is the last hole in the first row).

quality of fabrication procedure has improved, and the uniformity of the holes size is better than  $\pm 4 \text{ nm}$ . A periodic fluctuation of the hole size observed within each row can be attributed to the proximity effect during e-beam lithography step - the holes closer to the center of the structure receive bigger electron dose and therefore are slightly bigger.

### 3.2 Characterization of High-Q Cavities

Fabricated structures were tested at room temperature using micro-photoluminescence approach ( $\mu\text{PL}$ ). Due to poor heat sinking in our membrane-based devices, optical pumping was performed in pulsed regime, with limited duty cycles. In most cases structures were pumped with 1% duty cycles, using 10 ns pulses with 1  $\mu\text{s}$  periodicity, or 30 ns with 3  $\mu\text{s}$  periodicity. As the pump we used diode laser emitting at  $\lambda = 830 \text{ nm}$ . The pump beam was focused through 100x objective lens onto the sample surface to obtain a spot size of about  $2.5 \cdot 1.5 \mu\text{m}^2$ . The emission from the cavities was collected through the same lens, and the spectrum of the emitted signal was analyzed with an optical spectrum analyzer (OSA). Flip-up mirrors were used to obtain the optical images of the excitation pump-spot and the cavity modes.

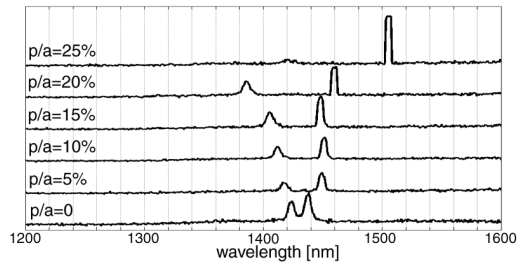


**Fig. 9** Position of resonant modes detected in cavities  $p_0 - p_5$  as a function of the elongation parameter  $p$ .  $r = 139$  nm,  $a = 434$  nm,  $r/a = 0.32$ ,  $r_{def}/a = 0.17$ .

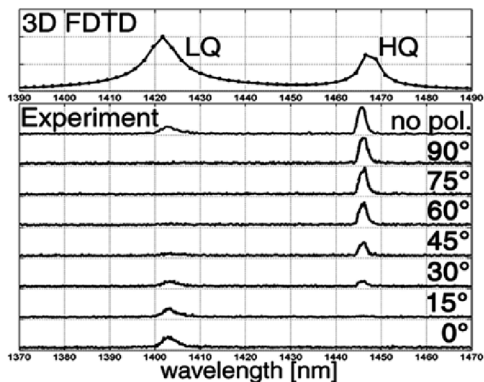


**Fig. 10** Polarization dependence of the resonant modes in  $p_3$  cavity.  $0^\circ$  corresponds to the y-axis direction.

First we measured the emission from the unprocessed InGaAsP material and obtained the gain spectrum of the active material. We found that emission exists between 1300 nm and 1650 nm, with a maximum at around 1550 nm. Assuming the lattice constant of  $a = 436$  nm (as in the case of the most of the fabricated structures) this wavelength range corresponds to normalized frequencies of  $a/\lambda \in (0.264, 0.335)$ , which is within the bandgap of the bulk photonic crystal mirrors surrounding the cavity. As the next step we tested all six cavities in one structure in order to characterize their resonant modes. We found two prominent resonant peaks in these cavities, all positioned within the bandgap of photonic crystal mirror<sup>†</sup> (Fig. 9). We also observed that the positions of these resonances depend strongly on the value of the elongation parameter  $p$ : originally double degenerate dipole modes of a single defect cavity ( $p_0$ ) become more split apart as amount of dislocation increases. This is the signature of the HQ and LQ modes of our cavity (Fig. 6). Slight variations in the case of structure  $p_5$  (peaks jump towards longer wavelengths) can be attributed to the variations in the defect hole size. Also, the splitting between LQ and HQ modes observed even in the case of  $p_0$  can be attributed to the broken symmetry of the structure due to the fabrication-related disorders.

In Fig. 10 we show polarization dependence of the two resonant modes of our cavity. It can be observed that two resonances are linearly polarized with orthogonal polarization. Moreover, the mode at longer wavelength (smaller fre-

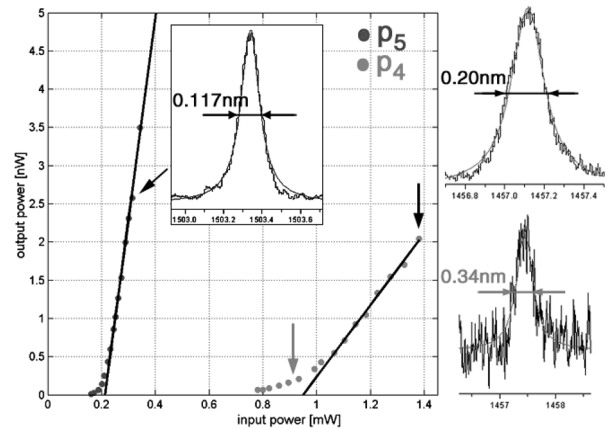


**Fig. 11** L-L curves for structures  $p_5$  and  $p_4$  pumped with  $DC = 1\%$ . Insets to the right show linewidth in  $p_4$  structure at two different pumping levels. Inset to the left shows resonant peak in  $p_5$  structure pumped above threshold.

quencies) is polarized along x-axis, and the one at shorter wavelength along y-axis, as expected in the case of HQ and LQ mode, respectively. In Fig. 10 we also show the position of the two modes as calculated using 3-D FDTD method. The results of numerical analysis are in excellent agreement with experiments<sup>††</sup>. According to theoretical predictions, for  $r_{def} \approx 0.15a$  (the case of fabricated structures), the Q is maximized when  $p = 0.25a$ . Therefore, we expect that the cavity  $p_5$  has the highest Q factors of all the fabricated structure and it is the best candidate for realization of low-threshold laser.

### 3.3 Room Temperature Laser

In Fig. 11 we show the dependence of emitted (peak) power a function of peak pump power [light-light (L-L) curve] for HQ resonant mode of  $p_5$  and  $p_4$  cavities. The pump power is the amplitude of the pump power at the sample surface, and the reflection from the sample is not taken into account. Therefore, actual power that “pumps” quantum wells is smaller. This is important to keep in mind when comparing pump powers reported in literature. When structure  $p_5$  is pumped with 1% duty cycle characteristic lasing curve is observed, with the threshold power as low as  $P_{th} = 214 \mu\text{W}$ . The linewidth above the threshold is reduced to only 0.117 nm, and was limited by the resolution of our OSA (0.1 nm). In the case of  $p_4$  cavity threshold occurs around  $P_{th} = 950 \mu\text{W}$ . There are two reasons for increased threshold in case of  $p_4$  cavity: (i) gain provided from quan-

<sup>†</sup>Relatively large linewidths of the resonances are due to the resolution bandwidth of OSA in this case ( $RB = 5$  nm). When measurements are taken with smaller resolution ( $RB < 1$  nm), linewidths are much narrower and limited by the Q of the cavities.

<sup>††</sup>Bigger linewidths observed in numerical simulation are due to the methodology of FDTD algorithm. In order to have sufficient resolution in frequency domain, many time-steps are required and FDTD simulation needs to be done for a long time (e.g., days/weeks). In most cases this is not practical and shorter calculations are performed, resulting in poor frequency resolution.

tum wells is smaller at this wavelength ( $\lambda = 1457.5$  nm) than in the case of  $p_5$  cavity ( $\lambda = 1504$ ) since gain peaks at  $\lambda \approx 1550$  nm and (ii) for  $r_{def} \approx 0.15a$  Q factor of  $p_4$  cavity is smaller than Q factor of  $p_5$ . In Fig. 11 we also show spectrum of the HQ peak of the  $p_4$  cavity, taken at the threshold. Full-width half-maximum of the resonance is  $FWHM = 0.34$  nm, and that corresponds to Q factor of  $Q \approx 4300$ . This is in good agreement with our theoretical predictions of  $Q_{p_4} = 4000$ . However, this high Q value that we measure should be taken with caution since the spectrum is taken at the threshold, and could be narrowed due to gain provided by quantum wells. We have measured  $Q \approx 2000$  for  $p_5$  cavity by measuring resonance linewidth far below threshold [11]. However, this is rather conservative value since it incorporates losses due to the reabsorption in the quantum wells. Also, we have measured  $Q \approx 2800$  in structures fabricated in quantum dot material [23].

### 3.4 Dense Integration of Laser

We have also tested structures with three different defect hole sizes ( $r_{def}/a$ ) within the same photonic crystal platform in order to explore the integration multi-wavelength photonic crystal lasers with lithographically predetermined spectra [Fig. 12(a)]. Geometry of the cavities are  $a = 446$  nm,  $r = 128$  nm,  $p/a = 20\%$ , and the sizes of the defect holes were  $r_{small} = 74$  nm,  $r_{mid} = 85$  nm and  $r_{big} = 97$  nm. The distance between the cavities is 10 lattice periods or  $\approx 4.5 \mu\text{m}$ .

The cavities were pumped individually and the emission from each nanocavity could be observed only when the pump beam was positioned exactly on top of the nanocavity. Even slight variations in the position of the pump beam resulted in turn-off of the laser. The lasing wavelength of

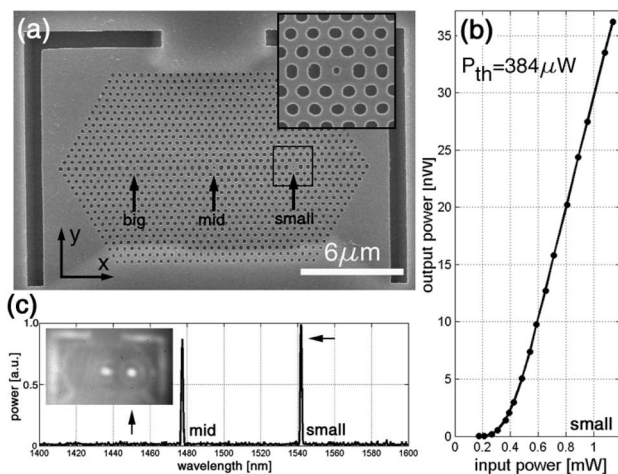


**Fig. 12** (a) Fabricated structure consists of three cavities integrated within the same photonic crystal mirror. Defect holes are indicated by arrows, and their size increases from right to left. (b) L-L curve for the laser with the smallest defect hole. (c) Simultaneous emission from two adjacent nanolasers (small and mid) pumped simultaneously using big (de-focused) pump spot. Inset shows image of the light emitted from nanolasers, and detected with IR camera. GaAs filter was used to cut off the pump beam.

the cavities could be tuned from  $\lambda = 1420$  nm (for  $r_{big}$ ) to  $\lambda = 1546$  nm (for  $r_{small}$ ). Figure 12(b) shows the L-L curve for the laser with  $r_{small} = 74$  nm, when that cavity was pumped locally, using focused pump beam. Threshold of this room temperature laser is  $P_{th} = 384 \mu\text{W}$ . We were also able to achieve simultaneous emission from two adjacent nano-lasers by de-focusing the pump beam so that the pump spot covers the whole structure shown in Fig. 12(a). The results are shown in Fig. 12(c). Emission from cavities with defect hole radius  $r_{small}$  and  $r_{mid}$  was detected, with comparable output powers. As it can be seen on image taken by our IR camera, the strong emission exists at positions of two nanocavities, only.

### 3.5 Near-Field Optical Microscopy

In order to confirm strong light localization to the defect cavity we have used near-field scanning optical microscope (NSOM) [24]. An illumination mode was used to pump the structures through the optical fiber tip, and the PL signal was detected through the reflective objective lens. The optical fiber tip was metal-coated and the aperture size at the end of the tip was 150 nm. The fiber tip is positioned at the dither piezo device and shear-force detector in order to control the distance between the tip and the sample surface ( $\approx 10$  nm) and to obtain a topographic image of the sample. The PPC nanocavities that we studied using NSOM are similar to those used to realize low-threshold lasers described in previous sections. The most important difference from the cavities analyzed so far was the omission of central defect hole, what results in Q-factors limited to about 1000. We did not observe lasing action in these cavities. Cavity parameters are  $a = 420$  nm,  $r/a = 0.32$ ,  $d/a = 0.79$  and  $p/a = 15\%$ .

In Fig. 13(a) we show the photo luminescence spectrum of the cavity, obtained using technique described in previous sections. Two peaks positioned around  $\lambda =$

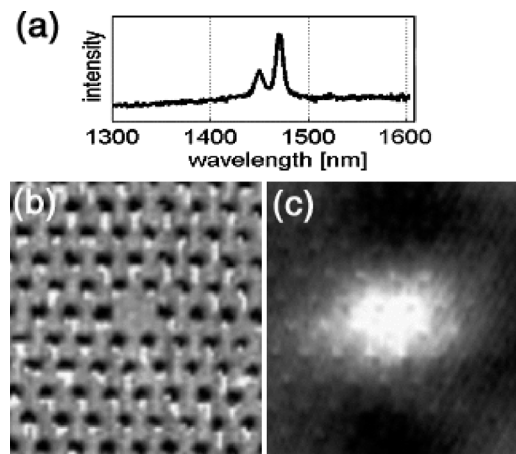


**Fig. 13** (a) Resonances detected using micro PL setup. Confined modes (around 1450 nm) and extended dielectric band modes (above 1600 nm) can be seen. (b) Topographic and (c) near-field optical image. Detected optical field corresponds to the confined cavity modes.

1450 nm correspond to the localized LQ and HQ dipole modes. In Figs. 13(b) and (c) we show the topographic image of the cavity and optical image of the cavity modes, respectively. The bright spot seen in optical image is located at the position of the defect cavity, as shown in topographic image. We have attributed this optical signal to the mixture of HQ and LQ dipole modes of our cavity. The size of the bright spot is roughly  $4.4ax3a$ . This small spot size is an indication of a small mode volume, as expected from the localized cavity modes. However, since these NSOM-PL results are obtained using illumination mode, the size of the cavity modes is over-estimated since the optical signal contains information on the diffusion properties of free carriers excited by the pump beam. Work is in progress to obtain *real* high-resolution image of the mode profile using collection mode of the NSOM (cavities pumped using the reflective lens, and signal collected using the fiber).

### 3.6 Photonic Crystal Nanolasers as Chemical Sensors

Until now, the applications of planar photonic crystals have been restricted to large-scale integration of optical wavelength division multiplex (WDM) components for telecommunications. Recently, we proposed application of planar photonic crystal cavities in the development of chemical sensors [13], with high spectral resolution and excellent sensitivity to changes in the refractive index of their surrounding. Our porous cavity design permits the introduction of analyte directly into the high optical field of the laser cavity, and, due to the ultrasmall mode volume of our lasers, permits the sensitivity to optical changes within  $\approx 100$  femtoliter volumes. The introduction of molecules into such cavities is expected to have a large influence on the optical signature, and the high fields obtained in the cavity can be used for spectroscopy of the cavity contents (e.g., Raman or absorption spectroscopy).

The simplest method of optically sensing ambient material uses wavelength shifts in the laser spectrum to measure refractive index of ambient. In this method, the sensitivity of the sensor depends on the smallest change in refractive index that can be optically detected. In *passive* devices, this is related to the width of the cavity resonance peak which in turn is determined by cavity quality  $Q$ . However, a laser linewidth can be much narrower than the passive cavity resonance, and even smaller shifts in the lasing wavelength can be detected by taking advantage of the spectral narrowing from stimulated emission above laser threshold.

To test the influence of a change in ambient refractive index on the laser spectrum of a cavity, we have backfilled our photonic crystal lasers with isopropyl alcohol (IPA) and methanol (Fig. 14). It can be seen that wavelength shifts of up to 67 nm can be observed when a cavity is immersed in IPA. This red-shift corresponds to a change in refractive index from 1.0 to 1.377, and yields roughly 1 nm spectral shift for a 0.0056 change in refractive index. When IPA is replaced with methanol ( $n = 1.328$ ), the laser resonance ex-

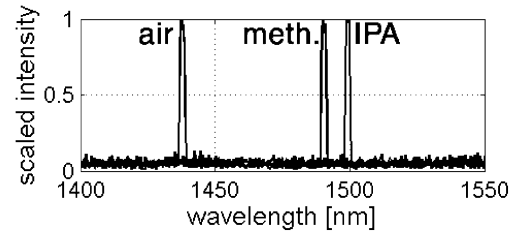


Fig. 14 Spectrum of the laser immersed in air, methanol and IPA.

periences a blue shift of  $\approx 9$  nm, which is again in good agreement with predicted shift of  $\approx 13$  nm from our theoretical predictions [13]. After the immersion in IPA laser threshold power was reduced from  $\approx 1$  mW to  $\approx 0.75$  mW, even though  $Q$  factor of the cavity backfilled with IPA is almost 6 times smaller than of the cavity suspended in air [13]. This can be attributed to better wavelength match with the gain spectrum of the quantum wells when cavity is immersed in IPA.

## 4. Conclusions

We have presented the design, fabrication and characterization of high- $Q$  photonic crystal nano-cavities. 3-D FDTD method is used as a design tool, and e-beam lithography followed by several dry and wet etching steps is used to fabricate cavities in InGaAsP material system. Room temperature lasing is observed from the high  $Q$  dipole modes of these nanocavities. In spite of the unusual design of our structures, which have a hole etched through the position of maximum field intensity and therefore reduced overlap with gain material, we observe low threshold powers in our devices. We have attributed this to the small mode volume and the high  $Q$  factors inherent to our device design. Polarization and lithographic tuning properties of two dipole modes supported in the cavity are in excellent agreement with theoretical FDTD predictions. The mode profile taken by our IR camera as well as using near-field scanning optical microscope confirms that the cavity resonance is well localized to the center of our cavity.

In nanolaser that we have developed high-intensity optical field is localized in the air. This is fundamentally different from the majority of semiconductor lasers, since they confine the light in the high-index material. Therefore, our lasers are ideally suited for investigation of interaction between light and matter placed in the high optical fields, and they provide us with opportunities for realization of integrated optical spectroscopy systems. We have demonstrated this concept and showed that changes in refractive index of the ambient surrounding the laser cavities can be measured by observing the shifts in emission wavelengths of the lasers. Since InGaAsP can serve both as a laser gain material as well as a material for light detection, it is possible to develop compact and integrated spectroscopy systems for detection of chemical and biological molecules.

## Acknowledgements

The authors would like to thank Dr. Sam Keo (Jet Propulsion Laboratory) for help in the lab, as well as Brett Maune (Caltech) for proofreading the manuscript. This work was supported by the NSF, AFOSR and Cross Enterprise Technology Development Program at JPL.

## References

- [1] E. Yablonovitch, "Inhibited spontaneous emission in solid-state physics and electronics," *Phys. Rev. Lett.*, vol.58, pp.2059–2062, May 1987.
- [2] S. John, "Strong localization of photons in certain disordered dielectric superlattices," *Phys. Rev. Lett.*, vol.58, pp.2486–2488, 1987.
- [3] T. Krauss, R. DeLaRue, and S. Brand, "Two-dimensional photonic-bandgap structures operating at near infrared wavelengths," *Nature*, vol.383, no.6602, pp.699–702, 1996.
- [4] T. Baba, "Photonic crystals and microdisk cavities based on gainaspinp system," *IEEE J. Sel. Top. Quantum Electron.*, vol.3, no.3, pp.808–830, 1997.
- [5] O. Painter, R. Lee, A. Scherer, A. Yariv, J. O'Brien, P. Dapkus, and I. Kim, "Two-dimensional photonic band-gap defect mode laser," *Science*, vol.284, no.5421, pp.1819–1821, 1999.
- [6] R. Lee, O. Painter, B. Kitzke, A. Scherer, and A. Yariv, "Photonic bandgap disk laser," *Electron. Lett.*, vol.35, no.7, pp.569–570, 1999.
- [7] H. Park, J. Hwang, J. Huh, H. Ryu, Y. Lee, and J. Kim, "Nondegenerate monopole-mode two-dimensional photonic band gap laser," *Appl. Phys. Lett.*, vol.79, no.19, pp.3032–3034, 2001.
- [8] C. Monat, C. Seassal, X. Letartre, P. Viktorovitch, P. Regreny, M. Gendry, P. Rojo-Romeo, G. Hollinger, E. Jalaguier, S. Pocas, and B. Aspar, "InP 2D photonic crystal microlasers on silicon wafer: Room temperature operation at 1.55  $\mu\text{m}$ ," *Electron. Lett.*, vol.37, no.12, pp.764–766, 2001.
- [9] H. Ryu, S. Kim, H. Park, J. Hwang, Y. Lee, and J. Kim, "Square-lattice photonic band-gap single-cell laser operating in the lowest-order whispering gallery mode," *Appl. Phys. Lett.*, vol.80, no.21, pp.3883–3885, 2002.
- [10] T. Yoshie, O. Shchekin, H. Chen, D. Deppe, and A. Scherer, "Quantum dot photonic crystal lasers," *Electron. Lett.*, vol.38, no.17, pp.967–968, 2002.
- [11] M. Lončar, T. Yoshie, A. Scherer, P. Gogna, and Y. Qiu, "Low-threshold photonic crystal laser," *Appl. Phys. Lett.*, vol.81, no.15, pp.2680–2682, 2002.
- [12] P. Lee, J. Cao, S. Choi, Z. Wei, J. O'Brien, and P. Dapkus, "Room-temperature operation of VCSEL-pumped photonic crystal lasers," *IEEE Photonics Technol. Lett.*, vol.14, no.4, pp.435–437, 2002.
- [13] M. Lončar, A. Scherer, and Y. Qiu, "Photonic crystal laser sources for chemical detection," *Appl. Phys. Lett.*, vol.82, no.26, pp.4648–4650, 2003.
- [14] S. Noda, A. Chutinan, and M. Imada, "Trapping and emission of photons by a single defect in a photonic bandgap structure," *Nature*, vol.407, no.6804, pp.608–610, 2000.
- [15] J. Vučković, M. Lončar, H. Mabuchi, and A. Scherer, "Design of photonic crystal microcavities for cavity QED," *Phys. Rev. E*, vol.65, no.1, p.016608, 2002.
- [16] J. Geremia, J. Williams, and H. Mabuchi, "An inverse-problem approach to designing photonic crystals for cavity QED," *Phys. Rev. E*, vol.66, no.6, p.06606, 2002.
- [17] O. Painter, J. Vučković, and A. Scherer, "Defect modes of a two-dimensional photonic crystal in an optically thin dielectric slab," *J. Opt. Soc. Am. B*, vol.16, no.2, pp.275–285, 1999.
- [18] J. Vučković and Y. Yamamoto, "Photonic crystal microcavities for cavity quantum electrodynamics with a single quantum dot," *Appl. Phys. Lett.*, vol.82, no.15, pp.2374–2376, 2003.
- [19] K. Srinivasan and O. Painter, "Momentum space design of high-Q photonic crystal optical cavities," *Opt. Express*, vol.10, no.15, pp.670–684, 2002.
- [20] E. Miyai and K. Sakoda, "Quality factor for localized defect modes in a photonic crystal slab upon a low-index dielectric substrate," *Opt. Lett.*, vol.26, no.10, pp.740–742, 2001.
- [21] A. Taflove, *Computational Electrodynamics—The Finite-Difference Time-Domain Method*, Artech House, Norwood, MA, 1995.
- [22] J. Vučković, M. Lončar, H. Mabuchi, and A. Scherer, "Optimization of the Q factor in photonic crystal microcavities," *IEEE J. Quantum Electron.*, vol.38, no.7, pp.850–856, 2002.
- [23] T. Yoshie, J. Vučković, A. Scherer, H. Chen, and D. Deppe, "High quality two-dimensional photonic crystal slab cavities," *Appl. Phys. Lett.*, vol.79, no.26, pp.4289–4291, 2001.
- [24] K. Okamoto, M. Lončar, T. Yoshie, A. Scherer, Y. Qiu, and P. Gogna, "Near-field scanning optical microscopy of photonic crystal nanocavities," *Appl. Phys. Lett.*, vol.82, no.11, pp.1676–1678, 2003.

**Marko Lončar** received the Diploma in Electrical Engineering from University of Belgrade, Serbia and Montenegro (1997) and M.S. (1998) and Ph.D. (2003) in Electrical Engineering from Caltech, USA. Currently, he is a postdoctoral scholar at Harvard University working in the group of Federico Capasso. His research interests are in the field of nanophotonics, including passive and active photonic crystal devices.

**Tomoyuki Yoshie** received the B.E. and M.E. degrees in Electrical Engineering from Kyoto University, Japan in 1990 and 1992, respectively, and the M.S. in Electrical Engineering from Caltech in 2000. He had been with Sanyo Electric from 1992 to 1999 for development of semiconductor lasers. He is currently working toward the Ph.D. degree at Caltech. His research interest is photonic crystal lasers.

**Koichi Okamoto** received the B.S. degree (1991) from the Faculty of Chemical Engineering, Doshisha University, Japan, and the M.S. (1994) and Ph.D. (1998) degrees from Department of Chemistry, Kyoto University, Japan. From 1998 until 2000 he was Researcher in Venture Business Laboratory, and from 2000 until 2002 he was Research Fellow of the Japan Society for the Promotion of Science, both at Kyoto University. Since 2001 he has been a Postdoctoral Scholar in Axel Scherer's group at Caltech, USA. His research interests include photo chemistry, optoelectronics, nonlinear optics, nanophotonics and development of highly time-spatial resolved spectroscopy.

**Yueming Qiu** received a B.S. (1986) and M.S. (1989) degrees from the Fudan University, Shanghai, and a Ph.D. (1993) from the Shanghai Institute of Technical Physics, Chinese Academy of Science. From 1994 to 1998, he was a postdoc and senior research associate of Henryk Temkin at Colorado State University and Texas Tech University. He joined Jet Propulsion Laboratory in 1998 and currently is a senior member of engineering staff responsible for MOCVD growth of III-V semiconductor materials. His research interests include the development of InP based DFB lasers for spectroscopic applications and InAs quantum dot optoelectronic devices.

**Jelena Vučković** is an assistant professor of Electrical Engineering at Stanford University. Before joining the faculty in January of 2003, she was a postdoctoral scholar in the Yamamoto Group also at Stanford University. She received the Ph.D. degree in 2002 from the Caltech for her work on photonic crystal-based optical and quantum optical devices. Her research interests span a number of experimental and theoretical topics in nanoscale photonics and quantum optics.

**Axel Scherer** received B.S., M.S. and Ph.D. degrees from the New Mexico Institute of Mining and Technology in 1981, 1982 and 1985 respectively. From 1985 to 1993 he worked in the Quantum Device Fabrication group at Bellcore. Currently, he is Bernard A. Netches professor of Electrical Engineering, Applied Physics and Physics at Caltech, USA. His research interests include design, fabrication and characterization of functional photonic, nanomagnetic and microfluidic devices.